Journal of Sol-Gel Science and Technology (2026)117:50
https://doi.org/10.1007/s10971-025-07085-w

ORIGINAL PAPER

Fabrication, characterization and adsorption of lead ions by doped barium hexaferrite nanoparticles

Ebtesam E. Ateia[1] · Yousra Yasser[1] · Amira S. Shafaa[1]

Received: 8 September 2025 / Accepted: 9 December 2025

Abstract

The citrate combustion technique was employed to synthesize barium hexaferrites represented by the formula $BaFe_{11.5}Y_{0.5}O_{19}$, where Y denotes Zr, Zn, Ni, and Gd. XRD analysis confirms the hexagonal structure of these materials, which are classified under the space group P63/MMC-(No 194). The smallest crystallite size is observed in $BaFe_{11.5}Gd_{0.5}O_{19}$, with measurements recorded at 36.968 nm according to the Halder-Wagner method. The band gap is calculated using the Tauc model. The introduction of dopant ions (Zr, Zn, Ni, and Gd) resulted in the establishment of electronic energy levels, which caused distortions in the sample and generated new locations for stabilizing charge carrier species within the samples. The BET plot shows H3 hysteresis with a type II isotherm, indicating that the inter-particle voids contribute to meso-porosity with an average pore diameter of 9.351 nm. The samples are applied in wastewater treatment, specifically serving as purifiers for lead-contaminated water. The impact of contact time is examined for all samples, revealing that $BaFe_{11.5}Zr_{0.5}O_{19}$ and $BaFe_{11.5}Gd_{0.5}O_{19}$ achieved the highest efficiencies of 99.693% and 99.237%, respectively. Moreover, $BaFe_{11.5}Zr_{0.5}O_{19}$ adhered to the intra-particle diffusion model, while $BaFe_{11.5}Zn_{0.5}O_{19}$, $BaFe_{11.5}Ni_{0.5}O_{19}$, and $BaFe_{11.5}Gd_{0.5}O_{19}$ correspond to the pseudo-second-order model, suggesting that the adsorption mechanism is primarily influenced by chemical processes.

✉ Ebtesam E. Ateia
drebtesam2000@yahoo.com
ebtesam@sci.cu.edu.eg

[1] Physics Department, Faculty of Science, Cairo University, Giza, Egypt

Published online: 05 February 2026

Graphical Abstract

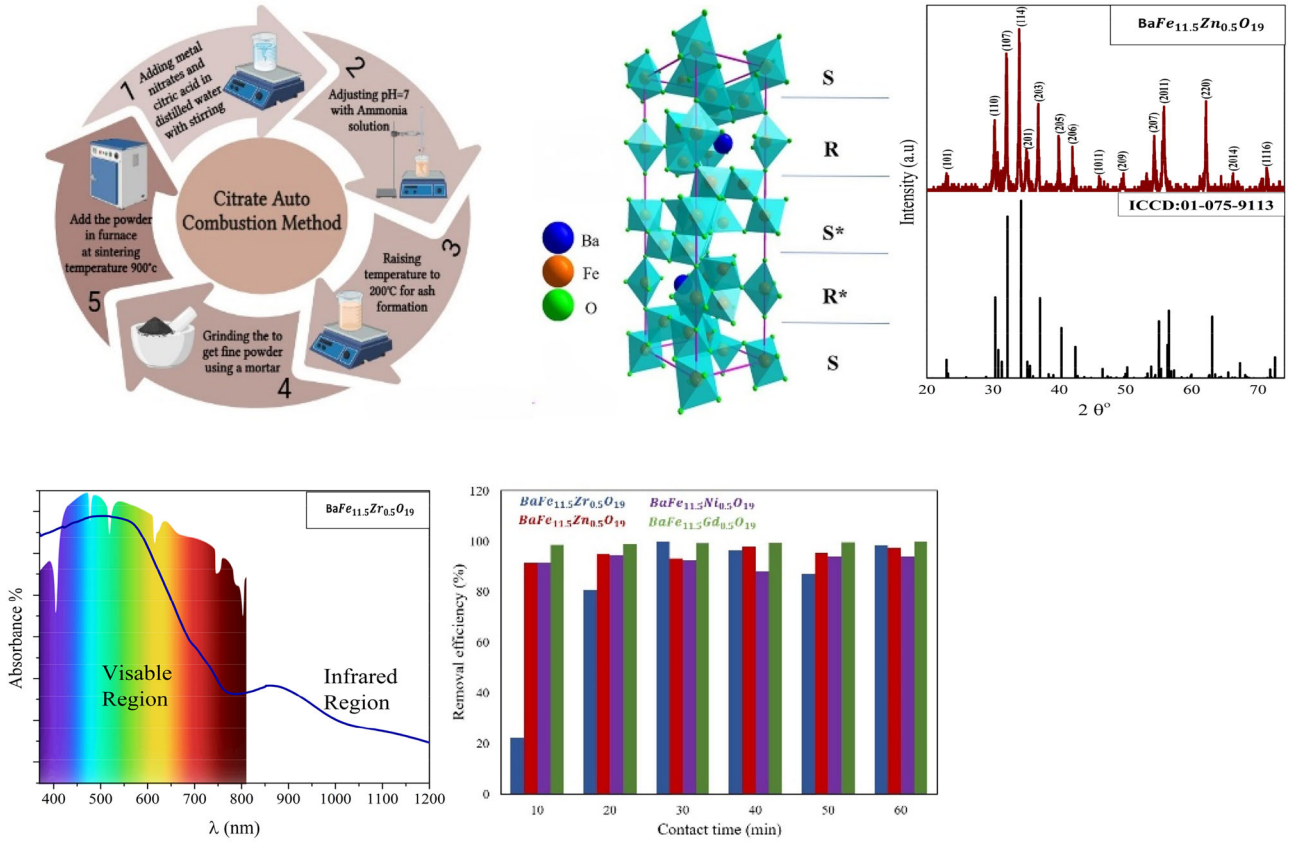

Keywords Magneto-plumbite structure, Isothermal models · Optical dispersion energy · Non-magnetic cations

Highlights

- The citrate autocombustion method was used to synthesize M-type barium hexaferrites (BHFs) with the general formula $BaFe_{11.5}Y_{0.5}O_{19}$
- The smallest crystallite size is observed in $BaFe_{11.5}Gd_{0.5}O_{19}$, with measurements of 35.328 nm according to the modified Scherrer model and 36.968 nm according to the Halder-Wagner approach.
- The substantial change in the refractive index "n" across the visible and near-infrared regions suggests that samples can be utilized in multilayer interference coatings.
- The prepared samples are employed in wastewater treatment, specifically as purifiers for lead-contaminated water.
- The impact of contact time is analyzed for all samples, revealing that $BaFe_{11.5}Zr_{0.5}O_{19}$ and $BaFe_{11.5}Gd_{0.5}O_{19}$ reached the highest efficiencies of 99.693% and 99.237%, respectively.

1 Introduction

Ferrite oxide nanomaterials are of interest for basic research as well as technological applications, owing to their crystal structure as demonstrated in Fig. 1a [1–6]. They have drawn substantial research attention due to their flexibility to alter physical properties via chemical modification and alternations in preparation conditions. The main benefit of ferrite nanomaterials (FNPs) is their straightforward preparation method [3, 6]. Among various ferrite substances, barium hexaferrite (BHF) and its derivative materials are commonly utilized in magnetic applications such as ferrofluids, sensors, permanent magnets, etc. [7–9]. It is important to note that BHF is the most appropriate candidate among magnetic materials due to its extreme corrosion resistance, high Curie temperature, high electrical resistivity, high saturation magnetization and large coercive field [3–5].

Researchers are modifying the physical properties of BHF through numerous processes, such as substituting appropriate elements at Ba/Fe sites, utilizing different

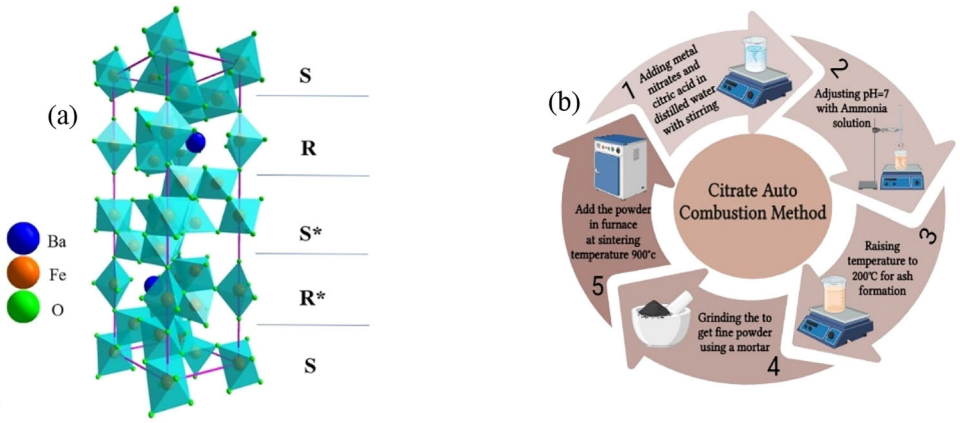

Fig. 1 **a** Diagram shows the crystal structure of BHFs, **b** Chart for citrate autocombustion method

preparation processes, and/or sintering at various temperatures [3]. There are various synthesis methods available for the synthesis of different FNPs, including citrate autocombustion techniques, co-precipitation method, sol-gel autocombustion method, etc. [5, 6]. However, numerous challenges are encountered in achieving high-purity homogeneous BHF NPs. To overcome these challenges, advanced citrate methods were employed [10, 11]. This combustion technique is less complex compared to others, making it appropriate for the preparation of BHF samples in the present study.

The increasing levels of heavy metals (HMs) in our resources have become a considerable concern, specifically as several industries are discharging metal-containing effluents into freshwater without appropriate treatment [12, 13]. Efforts have been made to eliminate or at least diminish the concentration of HMs such as lead (Pb^{2+}), and others from wastewater [14, 15]. HMs, like Pb^{2+} can enter surface waters through industrial effluents, furthermore, they can also enter the human body through ingestion and inhalation. Once inside the body, a significant portion of lead accumulates in the kidneys and liver, producing serious damage to these organs [16, 17]. Numerous approaches have been utilized to remove HM ions from wastewater, such as adsorption, cation-exchange, and electrochemical reduction, etc. [12, 18]. In general, the adsorption process is recognized for its cost, simplicity and flexibility, and hence has been industrially preferred [12]. Adsorption takes place owing to the physical or chemical attraction between Pb^{2+} ions and the surface of the prepared sample [19].

Recently, the innovation of sophisticated materials exhibiting improved physical characteristics has attracted considerable interest in the field of materials science. BHFs are increasingly recognized for their distinctive structure and optical features. A fundamental approach to modifying its crystal structure and improving its optical performance involves doping with cations that exhibit varying properties. This research aims to deliver a comprehensive understanding of how the partial substitution of Fe^{3+} with Zr^{4+}, Zn^{2+}, Ni^{2+} and Gd^{3+} cations influences the physical properties of BHF, ultimately aiding in the development of more effective materials for application in water treatment processes.

2 Methodology

2.1 Materials used

All chemicals Ba $(NO_3)_3{\cdot}6H_2O$ (99%), Zr $(NO_3).6H_2O$ (98%), Zn $(NO_3)_2.6H_2O$ (99.9%), Ni $(NO_3).6H_2O$, Gd $(NO_3)_2.6H_2O$ (99%), Fe $(NO_3)_3{\cdot}6H_2O$ (98%), citric acid $[C_4H_8O_7]$, and ammonia solution (33%) were taken from (LOBA, India).

2.2 Experimental technique

2.2.1 Preparation of barium hexaferrites (BHFs)

BHF NPs were synthesized using the citrate autocombustion method as illustrated in Fig. 1b. The chart depicts the preparation of the samples investigated in previous studies [10, 13, 14].

2.2.2 Preparation of heavy metals (HMs) solution

To investigate the effectiveness of $BaFe_{11.5}Y_{0.5}O_{19}$; $Y = Zn^{2+,}$ Zr^{4+}, $Ni^{2+,}$ and Gd^{3+} in removing HM ions, the experiments were conducted in a series of 500 mL flasks with 1.6 g/L of nanomaterial powder and 2ppm of metal nitrate. The solutions were thoroughly mixed using an electric shaker (ORBITAL SHAKER SO1) at 200 rpm for 60 minutes at room temperature. The resulting supernatant solutions were filtered through a 0.2 µm syringe filter. To

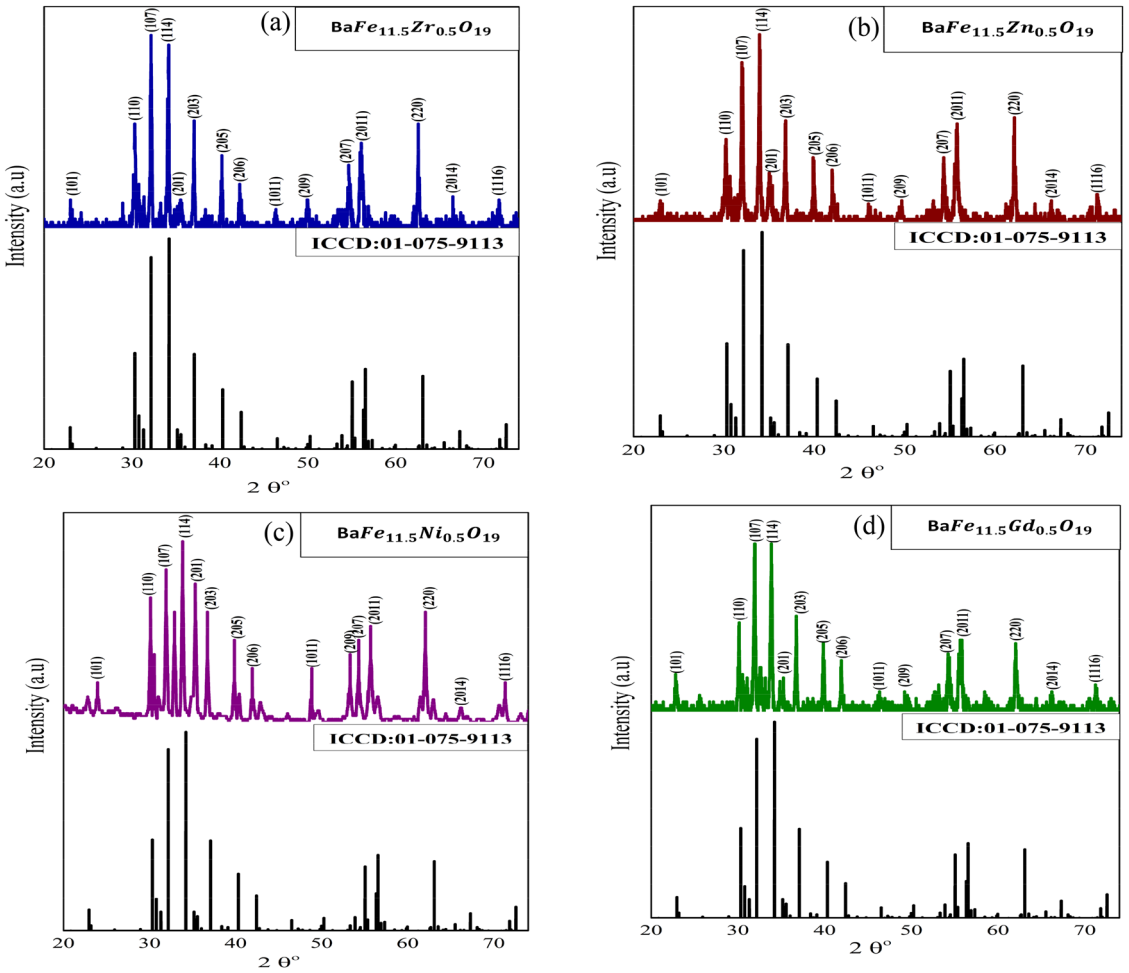

Fig. 2 The XRD patterns of the samples compared by ICCD card for **a** $BaFe_{11.5}Zr_{0.5}O_{19}$, **b** $BaFe_{11.5}Zn_{0.5}O_{19}$, **c** $BaFe_{11.5}Ni_{0.5}O_{19}$, **d** $BaFe_{11.5}Gd_{0.5}O_{19}$

study the effect of contact time, optimum pH values and adsorption techniques for the removal of heavy metal (RHM) Pb^{2+}, experiments were conducted following the procedures outlined in a previous study [20]. The concentration of Pb^{2+} ion was determined using atomic absorption spectrophotometry (ICP spectrometry Prodigy 7). The adsorption efficiency % and the equilibrium adsorption capacity (q_e) of metal ions were estimated for the samples in the forthcoming data.

2.3 Characterizations and measurements

The prepared samples were characterized using XRD to recognize the phase and study the crystal structure. FT-IR was used to determine the vibrational bands. EDXA showed the appearance of elements with compatible ratios. UV–vis was used for the optical characterizations of the synthesized materials.

3 Results and discussion

3.1 Structural analyses

3.1.1 XRD analysis

Figure 2 presents XRD patterns of $BaFe_{11.5}Zr_{0.5}O_{19}$, $BaFe_{11.5}Zn_{0.5}O_{19}$, $BaFe_{11.5}Ni_{0.5}O_{19}$ and $BaFe_{11.5}Gd_{0.5}O_{19}$ hexaferrites, ordered by their ionic radii; from the narrowest to the widest. XRD analysis confirms the presence of the desired hexagonal structure with all peaks matching the standard theoretical pattern of pure BHF with index number (ICSD 01-075-9113). In the figure, all sets of samples exhibit a single-phase structure, except $BaFe_{11.5}Ni_{0.5}O_{19}$, which shows an impurity peak corresponding to Fe_2O_3 (a secondary phase) [5, 6]. The sample $BaFe_{11.5}Gd_{0.5}O_{19}$, with the lowest 2θ value, corresponds to the smallest crystallite size, as shown in Table 1. The main peak (114) is slightly

Table 1 Crystallite size (D_s) with MSM and (D_H) from HWA compared with ionic radii (r) of the dopants, strain (ε) from HWA, experimental and theoretical density (ρ, ρ_x), porosity percentage (P %), specific surface area (S) of the prepared samples

Sample	r (Å)	D_S (nm)	D_H (nm)	ε *10^{-3}	$\rho_{exp.}$ (g/cm^3)	$\rho_{theo.}$(g/cm^3)	P %	S (m^2/g) *10^2
$BaFe_{11.5}Zr_{0.5}O_{19}$	0.560	39.113	45.372	3.096	1.630	5.973	72	235
$BaFe_{11.5}Zn_{0.5}O_{19}$	0.680	37.901	40.019	3.000	1.675	5.343	68	266
$BaFe_{11.5}Ni_{0.5}O_{19}$	0.690	35.630	37.495	2.986	1.804	5.274	65	295
$BaFe_{11.5}Gd_{0.5}O_{19}$	0.938	35.328	36.968	0.726	1.691	5.512	69	293

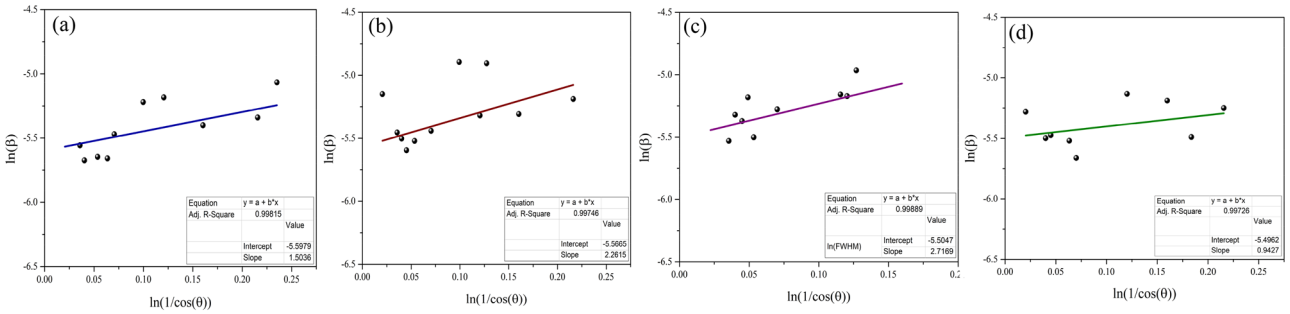

Fig. 3 The MSM plot for the samples: **a** $BaFe_{11.5}Zr_{0.5}O_{19}$, **b** $BaFe_{11.5}Zn_{0.5}O_{19}$, **c** $BaFe_{11.5}Ni_{0.5}O_{19}$, **d** $BaFe_{11.5}Gd_{0.5}O_{19}$

shifted to the left towards smaller 2θ values [5, 6]. This deviation from the typical trend is attributed to strain, which has been calculated and validated using the Halder-Wagner Approach (HWA). The strain estimated in the samples can be attributed to two factors: the introduction of larger doped ions entering the lattice, which occupy iron sites and lead to changes in valence, and the transformation of certain Fe^{3+} ions into Fe^{2+} ions that possess a larger radius [6, 21].

A variety of models have been established to interpret XRD data and derive significant insights. These models vary in their approaches to peak shape and the appropriate functions used to accurately fit the peaks, ensuring that all factors contributing to the creation of each peak are considered. Investigators frequently apply a combination of these models to recognize the material's structure and properties [15–17, 22]. In the present work, we have discussed two models: the modified Scherrer Model (MSM) and the Halder-Wagner approach (HWA).

The average crystallite size (D_S) of the prepared samples can be estimated via the MSM. This model supposes that the particles have a spherical shape [15] and that peak broadening is exclusively attributed to D_S without taking into account the strain factor (ε). In contrast, the HWA considers both instrumental and sample contributions to peak broadening [14, 15].

Table 1 indicates that the smallest calculated crystallite size is associated with the largest ionic radius of dopants. Consequently, $BaFe_{11.5}Zr_{0.5}O_{19}$ exhibits the largest crystallite size. Furthermore, the ε data calculated using the HWA model will support these findings. The Scherrer equation (MSM) was modified by Munshi et al. [15] as follows:

$$\ln\beta = \ln\left(\frac{1}{\cos\theta}\right) + \ln\frac{k\lambda}{D_s} \quad (1)$$

where β is the width of the diffraction line measured at its full half intensity, k is ≈ 0.94; and λ is the X-ray source wavelength. In the MSM, it is possible to acquire the average value of D_s through considering all peaks or a selected subset of peaks. Figure 3 illustrates the MSM plots, while the estimated values of D_s are tabulated in Table 1.

Researchers indicate that the summit of the peak corresponds to a Gaussian function (GF); however, the tail of the peak decreases too swiftly in accordance with a Lorentzian function (LF). The HWA posits that peak broadening arises from the convolution of both the LF and GF. The β can be represented as follows [10, 23]

$$\beta^2 = \beta_l\beta + {\beta_G}^2 \quad (2)$$

Accordingly, the HWA can be expressed as [14, 15]

$$\left(\frac{\beta^*}{d^*}\right)^2 = \frac{1}{D_H}\frac{\beta^*}{d^{*2}} + \left(\frac{\varepsilon}{2}\right)^2 \quad (3)$$

where β_l and β_G are the LF and GF peaks broadening, respectively, $\beta^* = \frac{\beta_{hkl}\cos\theta}{\lambda}$ and $d^* = \frac{2\sin\theta}{\lambda}$. A straight line is derived by plotting a graph between $\left(\frac{\beta^*}{d^*}\right)^2$ against $\frac{\beta^*}{d^{*2}}$ as shown in Fig. 4 which represents the HW plot. The 1/slope denotes the average "D_H", while the intersection is proportional to ε. The average D_H and ε are illustrated in Table 1. The average D_H values have the same trend as the D_S, suggesting that the change of ε affects the average D_H.

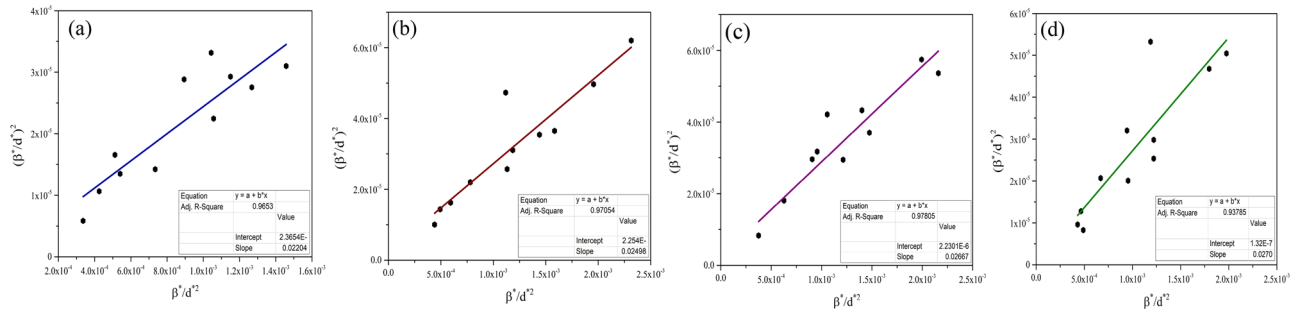

Fig. 4 The H-W approach plot for the samples: **a** $BaFe_{11.5}Zr_{0.5}O_{19}$, **b** $BaFe_{11.5}Zn_{0.5}O_{19}$, **c** $BaFe_{11.5}Ni_{0.5}O_{19}$, **d** $BaFe_{11.5}Gd_{0.5}O_{19}$

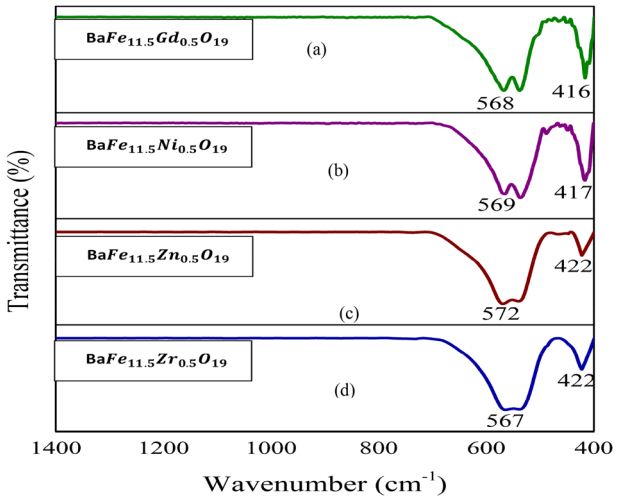

Fig. 5 The FT-IR spectrum of 400–1400 cm^{-1} of: **a** $BaFe_{11.5}Zr_{0.5}O_{19}$, **b** $BaFe_{11.5}Zn_{0.5}O_{19}$, **c** $BaFe_{11.5}Ni_{0.5}O_{19}$, **d** $BaFe_{11.5}Gd_{0.5}O_{19}$

The experimental density ($\rho_{exp.}$), is calculated by using the following formula

$$\rho_{\exp.} = \frac{m}{V} \tag{4}$$

The theoretical density ($\rho_{theo.}$) and porosity (P %) of the samples, are determined through the equations provided in references [24, 25],

$$\rho_{theo.} = \frac{Z\,M}{N_A\,V_x} \tag{5}$$

$$P = \left(1 - \frac{\rho_{\exp.}}{\rho_{theo.}}\right) * 100 \tag{6}$$

where m and V are the mass and volume of the samples (the bulk volume of the sample in the form of a sphere can be determined by geometric means using a caliper.), Z is the effective number of molecules per unit cell ($Z = 2$), M is the molecular weight, *and* $N_A = 6.026x10^{23}$/mole is Avogadro's number. The density of each sample mainly varies with the molar mass of each substituted cation. The sample with the largest molar mass, such as $BaFe_{11.5}Zr_{0.5}O_{19}$, has the highest density. This property is useful for many applications, such as wastewater treatment.

The change in P (Table 1) for doped BHF is due to the substitution of Fe^{3+} cation with cations of varying ionic radii, shape, size, and distribution within the crystallographic sites. This led to the creation of the highest porous $BaFe_{11.5}Zr_{0.5}O_{19}$ (72%) sample which appropriate for numerous applications [6]. The $\rho_{theo.}$ of all samples is higher than their $\rho_{exp.}$ indicating the existence of pores and good packing during preparation and calcination. The non-linear porosity values of the doped samples may be ascribed to agglomerations and grain growth in the synthesized NPs.

Additionally, the specific surface area (S) is calculated using the following equations [19],

$$S = \frac{6000}{\rho_{theo.} D_x} \tag{7}$$

As indicated in the table, larger crystallite sizes are associated with a smaller S. This behavior emphasizes the significant role of sizes in the surface characteristics of the samples

3.1.2 FT-IR analysis

The FT-IR spectra for the doped samples are illustrated in Fig. 5a–d. All samples exhibit three prominent absorption bands within the range of 400–1400 cm^{-1}, which are attributed to the metal-oxygen stretching vibration bands of Fe–O or Ba–O [10, 15]. The bands located at ≈430 and 580 cm^{-1} are associated with the vibrations of ferric crystallographic sites $4f_2$ and $4f_1$ (B and A sites). The absorption peak detected at 540 cm^{-1} is clearly linked to the Ba–O stretching vibration band, thus confirming the establishment of an M-type BHF structure. The identified band positions in the observed IR spectrum of $BaZr_{0.5}Fe_{11.5}O_{19}$ and $BaZn_{0.5}Fe_{11.5}O_{19}$ samples show a slight shift towards higher wavenumbers, compared to $BaNi_{0.5}Fe_{11.5}O_{19}$ and $BaGd_{0.5}Fe_{11.5}O_{19}$. These shifts in bands suggest changes in Fe^{3+}–O^{2-} bond lengths, which are attributed to differences

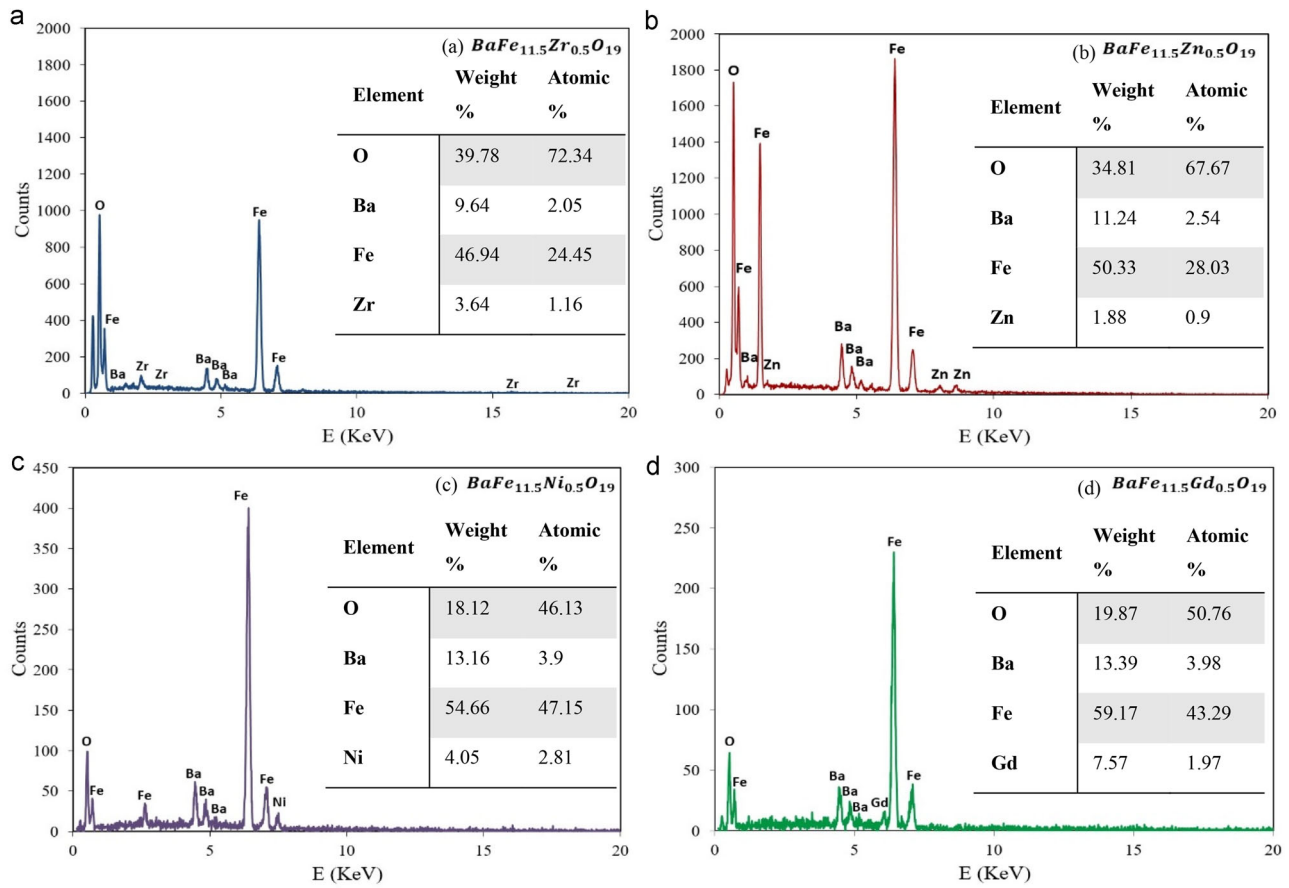

Fig. 6 EDX Spectra of: **a** $BaFe_{11.5}Zr_{0.5}O_{19}$, **b** $BaFe_{11.5}Zn_{0.5}O_{19}$, **c** $BaFe_{11.5}Ni_{0.5}O_{19}$, **d** $BaFe_{11.5}Gd_{0.5}O_{19}$

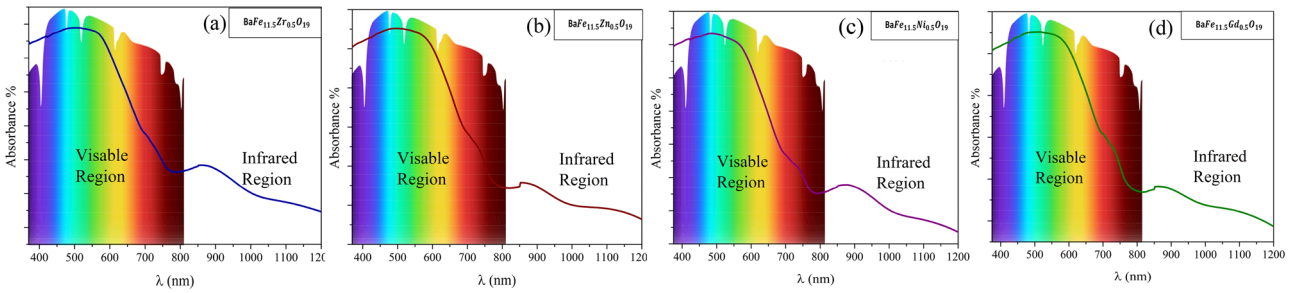

Fig. 7 Absorbance spectrum of: **a** $BaFe_{11.5}Zr_{0.5}O_{19}$, **b** $BaFe_{11.5}Zn_{0.5}O_{19}$, **c** $BaFe_{11.5}Ni_{0.5}O_{19}$, **d** $BaFe_{11.5}Gd_{0.5}O_{19}$

in ionic radius, Fe–O bond distances, and the heavier atomic weight of Fe^{3+} [11, 14, 21].

Finally, the substitution of: Zr^{4+}, Zn^{2+}, Ni^{2+} and Gd^{3+} ions into the Fe^{3+} site produces lattice strain, supporting the results obtained from XRD [23, 26].

3.1.3 EDX analysis

EDX is a valuable technique for determining the elemental composition and spatial distribution of BHFs. The EDX spectra shown in Fig. 6 present the elements for each sample in the desired ratios, mainly the atomic ratio of oxygen, which plays a main role in the presence of oxygen vacancies. No impurity peaks have been detected, confirming the purity of the synthesized samples [7].

3.2 Optical studies

3.2.1 Absorbance and optical energy bandgap

Figure 7 shows the absorbance spectrum with respect to the wavelength (λ) for the doped materials in the UV to IR

regions. The studied samples exhibit the same behavior with absorbance increasing as the λ increases until it reaches a maximum at 490, 496, 500 and 513 nm for $BaFe_{11.5}Zr_{0.5}O_{19}$, $BaFe_{11.5}Zn_{0.5}O_{19}$, $BaFe_{11.5}Ni_{0.5}O_{19}$ and $BaFe_{11.5}Gd_{0.5}O_{19}$, respectively, after which it decreases. The doped samples displayed broad absorption bands with peaks that shifted to higher λ, as their ionic radii increased. This indicates that the energy necessary to promote an electron across the band gap is weakening, thereby suggesting a reduction in the optical energy gap (E_g).

The E_g of studied samples can be influenced by their ionic radii. Typically, the ion with the smallest ionic radius ($BaFe_{11.5}Zr_{0.5}O_{19}$) is associated with the largest E_g, as demonstrated in Table 2. This phenomenon occurs because smaller ions have higher ionization energies, a higher charge density, greater crystal field splitting, and therefore, a higher energy necessary for an electron to transition from the valence band (V.B.) to the conduction band (C.B.). This suggests that as the ionic radii increase, materials become easier to excite optically as seen in the $BaFe_{11.5}Gd_{0.5}O_{19}$ sample. However, this relationship can be affected by various issues including crystal structure, coordination number, and the presence of defects. In mixed ionic compounds, the interaction of various ionic radii may result in differences in the E_g. For instance, in BHF NPs, the dimensions of the five site cations can greatly affect the E_g.

The optical properties of any material can be determined through band-gap analysis. This can be changed through doping or substitution to improve the material's applicability for opto-electronic devices [27]. The Eg can be derived from a UV-visible absorption spectrum, using the relationship between reflectance (R) and absorption as described by the Kubelka–Munk function.

$$F(R_\infty) = \frac{(1-R)^2}{2R} \tag{8}$$

where R is the reflectance of the sampled layer.

The Tauc method is a more straightforward approach that focuses on analyzing specific parts of the spectrum to estimate the Eg. The E_g as a function of λ is determined by extrapolating the linear segment of Tauc's plot illustrated in Fig. 8 in accordance with Eq. (9)

$$h\nu F(R_\infty) = B(h\nu - E_g)^m \tag{9}$$

where B is a constant and m depends on the type of transition, m = ½, m = 2 for direct and indirect transitions, respectively. The direct E_g values for the prepared samples are presented in Table 2. The changes in E_g align with those documented earlier and suggest that doping has a significant effect on the E_g of the BHFs. Nevertheless, the alteration in E_g can be attributed to two issues: the emergence of additional defects like oxygen vacancies and the ionic radii of the samples [28, 29]. The incorporation of dopant ions (Zr, Zn, Ni, and Gd) led to the formation of electronic energy levels, which induced distortions within the sample and created new sites for stabilizing charge carrier species in the doped material. This can either increase or decrease the E_g depending on the type and concentration of the dopant as will be discussed later.

The absorption spectrum fitting procedure (ASF) method takes a more comprehensive and statistical approach to fit the entire absorption spectrum. It includes parameters such as the density of states, transitions between bands, and the effects of localized states to match the entire absorption spectrum rather than selecting specific regions. It is employed to achieve the Eg, thereby eliminating the necessity for thickness measurements that are commonly imprecise. To present the ASF method, one may begin with Eq. (9) and reformulate it as a function of the λ [29, 30]

$$F(R_\infty) = B\,(hc)^{m-1}\lambda\left(\frac{1}{\lambda} - \frac{1}{\lambda_g}\right)^m \tag{10}$$

Table 2 Ionic radii, Energy bandgap (E_g) by Tauc's and ASF models, of the doped samples

Sample	r (Å)	E_g Tauc (eV)	E_g ASF (eV)
$BaFe_{11.5}Zr_{0.5}O_{19}$	0.560	1.728	1.590
$BaFe_{11.5}Zn_{0.5}O_{19}$	0.680	1.704	1.587
$BaFe_{11.5}Ni_{0.5}O_{19}$	0.690	1.673	1.570
$BaFe_{11.5}Gd_{0.5}O_{19}$	0.938	1.646	1.543

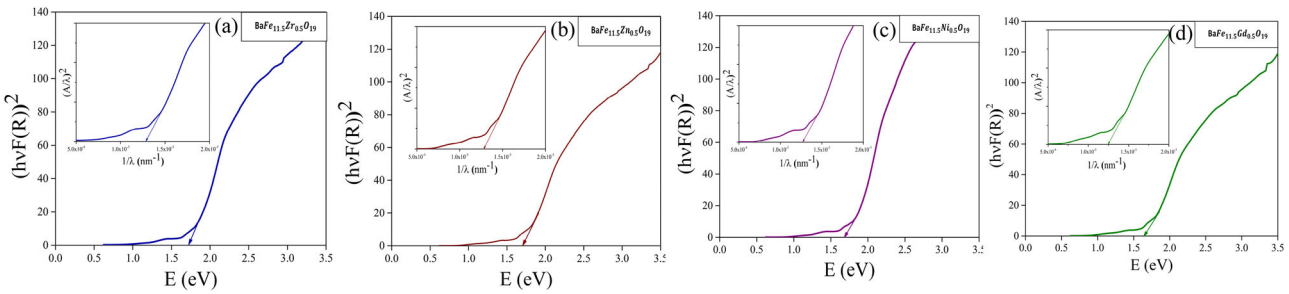

Fig. 8 Tauc's plot with ASF plot of: **a** $BaFe_{11.5}Zr_{0.5}O_{19}$, **b** $BaFe_{11.5}Zn_{0.5}O_{19}$, **c** $BaFe_{11.5}Ni_{0.5}O_{19}$, **d** $BaFe_{11.5}Gd_{0.5}O_{19}$

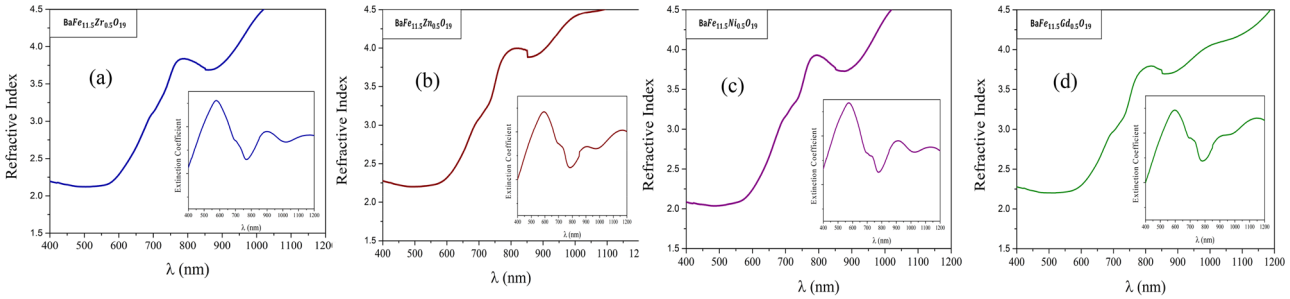

Fig. 9 The variation of n, and k, with λ for: **a** $BaFe_{11.5}Zr_{0.5}O_{19}$, **b** $BaFe_{11.5}Zn_{0.5}O_{19}$, **c** $BaFe_{11.5}Ni_{0.5}O_{19}$, **d** $BaFe_{11.5}Gd_{0.5}O_{19}$

where c is the velocity of light, λ, and λ_g are the wavelength, and bandgap wavelength, respectively. The values of $E_g{}^{ASF}$ are calculated from Fig. 8 and tabulated in Table 2, which shows the same trend as $E_g{}^{Tauc}$. The E_g has a strong dependence on the density of localized states. This tunability of the Eg makes BHF-doped materials extremely versatile for multifunctional applications in electronics, magnetics, optics, and energy fields, such as photocatalysis, magneto-optical sensors, and UV photodetectors. In conclusion, it can be stated that, based on the characteristics of the materials and the requirements of the experiments, the Tauc and ASF methods collectively provide a comprehensive description of the optical transitions occurring in HFs. Additionally, doping the crystal structure with Zr^{4+}, Gd^{3+}, Zn^{2+} and Ni^{2+} cations modifies the critical aspects of the sample's optical band structure. Such adjustments make BHF a valuable component for numerous technological uses [8, 25, 31–35].

3.2.2 Refractive index (n) and extinction coefficient (k)

The optical parameters characterize how electromagnetic waves transmit signals and travel through materials. However, there are two categories of dispersion based on the relationship between the refractive index (n) and wavelength (λ). Normal dispersion is characterized by an indirect proportionality between n and λ, occurring at λ below a certain threshold (corresponding to the resonance frequency, ω_o) [36].

Conversely, anomalous dispersion is defined by a direct relationship between n and λ, occurring at λ above this threshold [36]. This means n increases with increasing λ. The refractive index (n) is a significant parameter in optical applications. The formula utilized to compute n is as follows [30],

$$n = \frac{1+\sqrt{R}}{1-\sqrt{R}} \tag{11}$$

An anomalous dispersion in the variation of n is seen in Fig. 9. The anomalous dispersion observed between 700 and 900 nm arises from nearby electronic transitions associated with Fe^{3+} ions in $BaFe_{11.5}Zr_{0.5}O_{19}$. This anomaly occurs in regions that are very close to the strong absorption bands of the samples. In these regions, the electromagnetic wave interacts strongly with the hexaferrite's constituents, resulting in energy absorption and a rapid change in the speed of light within the medium. The unique crystal structure and ferrimagnetic nature of hexaferrites, where Fe^{3+} ions occupy five different sites with opposite spin alignments, lead to complex magnetic behaviors. These can result in strong spin rotations or ferromagnetic resonance within the material at specific frequency ranges, which cause significant absorption of electromagnetic energy. The detected behavior can be theoretically justified through the Kramers–Kronig relations [37] and can be modeled using the Lorentz–Drude dispersion model [38].

A significant difference exists between the doped samples as there is a reduction of n by passing through $BaFe_{11.5}Zn_{0.5}O_{19}$ to $BaFe_{11.5}Zr_{0.5}O_{19}$ ultimately achieving the lowest value of n in $BaFe_{11.5}Gd_{0.5}O_{19}$. Moreover, this anomalous behavior is associated with strong absorption. Materials that display this anomalous behavior are exemplified by moderate opacity at the resonance frequency and show anomalous dispersion within their absorption bands.

The substantial change in "n" across the visible and near-infrared regions suggests that samples can be utilized in multilayer interference coatings. The relatively high "n" achieved in the near-infrared region can be advantageous for manufacturing waveguides and photonic devices.

Additionally, the variation of the extinction coefficient (k) with λ is depicted in the inset of Fig. 9 and calculated using the following equation [30].

$$k = \frac{\alpha\lambda}{4\pi} \tag{12}$$

The absorption/scattering of light per unit volume is represented as k, indicating a decrease in light in each sample. The values of k increase with higher λ, suggesting increased absorption in the UV region due to direct electronic transitions. As λ decreases, k decreases due to reduced absorption. The large excitation energy for

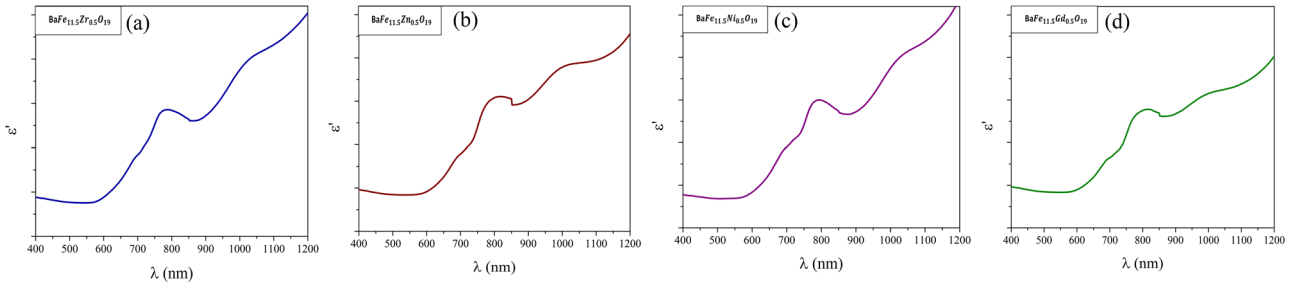

Fig. 10 The variation of dielectric constant with wavelength of **a** $BaFe_{11.5}Zr_{0.5}O_{19}$, **b** $BaFe_{11.5}Zn_{0.5}O_{19}$, **c** $BaFe_{11.5}Ni_{0.5}O_{19}$, **d** $BaFe_{11.5}Gd_{0.5}O_{19}$

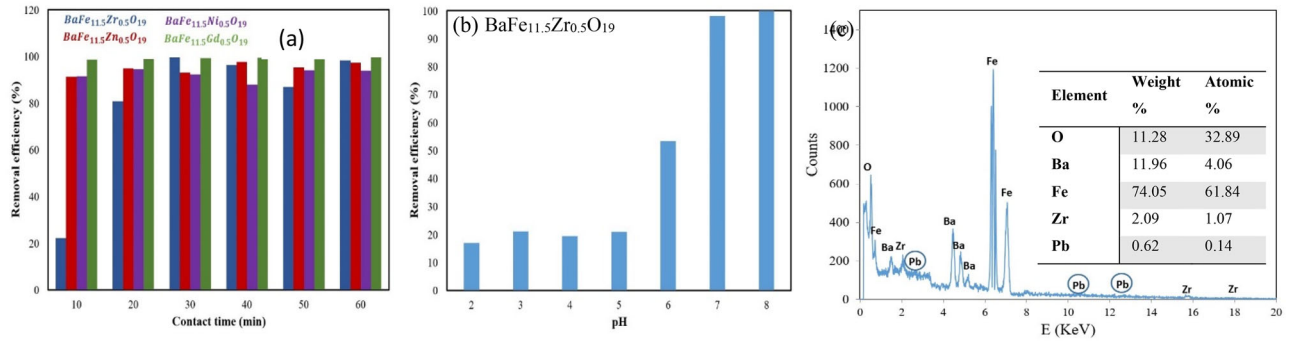

Element	Weight %	Atomic %
O	11.28	32.89
Ba	11.96	4.06
Fe	74.05	61.84
Zr	2.09	1.07
Pb	0.62	0.14

Fig. 11 **a** The removal efficiency with contact time for the prepared samples. **b** The removal efficiency with pH for $BaFe_{11.5}Zr_{0.5}O_{19}$. **c** EDXA for $BaFe_{11.5}Zr_{0.5}O_{19}$

electronic transitions results in strong inter-band optical transitions between the V.B and C.B. [36].

3.2.3 The dielectric constant (ε')

The real part of dielectric constant (ε') of materials can be linked to the values of n and k as the given equation [36, 39, 40],

$$\varepsilon'(\lambda) = n^2(\lambda) - k^2(\lambda) \tag{13}$$

The change of ε' as a function of λ is displayed in Fig. 10. As can be observed, the constant ε' has the same behavior as the "n" and is attributed to electronic polarization, a phenomenon that appears in heterogeneous media consisting of phases with different ionic conductivity [39]. The increase in ε', rises sharply, indicating a stronger response of the material's polarization to the oscillating electric field of the light. This suggests that electronic transitions are becoming more prominent as the wavelength increases. The bump near 750 nm indicates resonant interaction such as multiple polarization mechanisms or electronic transitions. The behavior of ε' makes the materials useful for photonic devices, capacitors and optical coatings.

3.3 Heavy metal removal (HMR)

The structural parameters obtained from XRD include size and strain. Additionally, the BET analysis provides information on surface area, pore size, and pore volume. All these parameters are closely related to the adsorption performance of the doped HFs. Smaller sizes lead to higher surface areas, which can increase the number of active sites available for adsorption and facilitate faster diffusion of Pb^{2+} ions toward the active sites on the HFs

On the other hand, strain creates defects in the crystal lattice of the HFs sample, which can serve as additional active sites for adsorption, and affect the binding energy of Pb^{2+} ions to the sample surface. Additionally, doping-induced distortions at grain boundaries create additional adsorption pathways.

3.3.1 Effect of contact time

In the present work, heavy metal concentrations (HMC) in the filtrate are measured using ICP, Prodigy7 at 25 °C. The nanomaterial removal efficiency is calculated as follows [30],

$$\text{efficiency}\% = \frac{C_i - C_e}{C_i} \times 100\% \tag{14}$$

where C_i and C_e are the initial and equilibrium (final) concentrations (mg/L) of metal ion solution, respectively, and plotted versus the time in Fig. 11 for the prepared samples.

A rapid elimination of Pb^{2+} ions is detected during the initial 30 min of adsorption, achieving removal efficiencies (η) of 99.7%, 93.1%, 92.4%, and 99.0% for $BaFe_{11.5}Zr_{0.5}O_{19}$, $BaFe_{11.5}Zn_{0.5}O_{19}$, $BaFe_{11.5}Ni_{0.5}O_{19}$, and $BaFe_{11.5}Gd_{0.5}O_{19}$, respectively. Subsequently, the adsorption kinetics slowed until reaching equilibrium at pH 8 after 60 min. The $BaFe_{11.5}Zr_{0.5}O_{19}$ sample exhibits the highest η (99.7%) despite its larger size. This can be attributed to its larger porosity (72%) and strain (3.096×10^{-3}). The combined effect of porosity and strain surpasses the effect of size on the absorption process. Based on these findings, $BaFe_{11.5}Zr_{0.5}O_{19}$ is selected for further investigation regarding the impact of pH on HMR.

3.3.2 Effect of pH

The impact of pH on the $BaFe_{11.5}Zr_{0.5}O_{19}$ sorption process of Pb^{2+} ions is examined within a pH range of 2–8 using ammonia and diluted nitric acid solutions, as shown in Fig. 11b. The primary interactions involved in the adsorption process are electrostatic in nature. The pH can affect the kinetics of adsorption and the sorption capacity of Pb^{2+} ions by varying the surface charges of $BaFe_{11.5}Zr_{0.5}O_{19}$, in addition to affecting the type of Pb^{2+} complex formed and the number of active sites available for the adsorption process. In the present investigation, the highest uptake of Pb^{2+} ions by $BaFe_{11.5}Zr_{0.5}O_{19}$ is detected at a pH value of 8, as illustrated in the figure [41]. This can be ascribed to a competition between H^+ and Pb^{2+} ions for adsorption on $BaFe_{11.5}Zr_{0.5}O_{19}$. At lower pH levels, H^+ ions tend to occupy an extensive number of adsorption sites on $BaFe_{11.5}Zr_{0.5}O_{19}$, thus hindering the Pb^{2+} adsorption process. Conversely, at high pH values, the competition from H^+ ions vanishe,s and the positively charged Pb^{2+} and $Pb(OH)^+$ ions can easily attach to the free binding sites, increasing the Pb^{2+} adsorption process [20, 22, 41].

3.3.3 Adsorption models

Adsorption isotherm and adsorption kinetics models are examined for the adsorption efficiency of Pb ions on $BaFe_{11.5}Zr_{0.5}O_{19}$, $BaFe_{11.5}Zn_{0.5}O_{19}$, $BaFe_{11.5}Ni_{0.5}O_{19}$ and $BaFe_{11.5}Gd_{0.5}O_{19}$ NPs. The equilibrium adsorption capacity of metal ions is determined as follows [20, 42],

$$q_e = \frac{C_i - C_e}{m} \times V \tag{15}$$

where V is the volume of Pb^{2+} solution (L) and m is the mass of adsorbent in grams. The mechanism of adsorption between the samples and the Pb^{2+} liquid phase can be identified with two models. The first one is the Langmuir isotherm model (LIM), and the other is the Freundlich model (FIM) [41]. The regression coefficient (R^2) is the parameter that supports these models. If the adsorption is portrayed as a mono-layer, it obeys the LIM with a finite number of alike sites on the surface of the adsorbent. Consequently, the equilibrium distribution of metal ions between the solid and liquid phases can be represented by the LIM re [20, 42]. The LIM follows the given equation [20],

$$\frac{C_e}{q_e} = \frac{1}{k_l q_m} + \frac{C_e}{q_m} \tag{16}$$

where q_e and q_m (mg/g) are the adsorption capacity at equilibrium and maximum adsorption, respectively. Ce is the equilibrium concentration of the metal ion (mg/L), and k_l (L/mg) is the affinity binding constant. The values of q_m and k_L are determined from the slope and intercept of the Langmuir plot.

The fundamental features of the LIM can be extracted through the equilibrium parameter (R_L), which is a dimension-less constant and given by [42],

$$R_L = \frac{1}{1 + (1 + k_L C_i)} \tag{17}$$

The R_L value indicates the adsorption nature to be unfavorable if $R_L > 1$. If $R_L = 1$ the process is linear. In case where $0 < R_L < 1$ the adsorption process is favorable as is the situation here. When $R_L = 0$ the process becomes irreversible [41, 42]. Additionally, by examining the correlation coefficients (R^2), it is evident that the experimental data align closely with LIM.

If the adsorption is multilayer, it obeys the FIM with a heterogeneous surface onto the adsorbent, and given by [20],

$$\ln q_e = \ln k_f + \frac{1}{n} \ln C_e \tag{18}$$

where k_f denotes the adsorption capacity and n represents the intensity of adsorption.

There are three kinetic models, the pseudo-first order (PFO), pseudo-second order (PSO) and interparticle diffusion (IPD) kinetic models. The PFO model is illustrated by physisorption, indicating the absence of a chemical bond between the adsorbent ($BaFe_{11.5}Y_{0.5}O_{19}$) and the adsorbate (Pb^{2+}). This reversible process is regulated by Van der Waals forces, where attraction adjusts with distance due to the continuous fluctuations in electron

Table 3 Calculated data of adsorption mechanism models for $BaFe_{11.5}Zr_{0.5}O_{19}$, $BaFe_{11.5}Zn_{0.5}O_{19}$, $BaFe_{11.5}Ni_{0.5}O_{19}$ and $BaFe_{11.5}Gd_{0.5}O_{19}$

Sample	q_e (mg/g)	Removal efficiency (%) within 30 min	Langmuir			Freundlich		PFO		PSO		IPD	
			k_L (L/mg)	R^2	R_L	k_F (mg/g)	R^2	k_1 (min^{-1})	R^2	k_2 (mg/g.min)	R^2	k_3 (mg/g.$min^{1/2}$)	R^2
$BaFe_{11.5}Zr_{0.5}O_{19}$	1.950	99.69	10.01	0.960	0.046	1.570	0.780	0.115	0.240	0.006	0.49	0.268	0.620
$BaFe_{11.5}Zn_{0.5}O_{19}$	1.910	93.09	285.50	0.990	0.001	1.640	0.960	0.115	0.280	0.587	0.99	0.022	0.640
$BaFe_{11.5}Ni_{0.5}O_{19}$	4.310	92.38	0.050	0.990	0.455	4.190	0.950	0.168	0.910	1.246	0.99	0.010	0.990
$BaFe_{11.5}Gd_{0.5}O_{19}$	1.840	99.23	77.00	0.990	0.006	1.510	0.980	0.002	0.050	1.284	0.99	0.002	0.010

distribution that create transient dipoles. It can be represented as follows [41],

$$\ln(q_e - q_t) = \ln q_e - \frac{k_1}{2.303} t \tag{19}$$

Moreover, the PSO commonly occurs when there is significant interaction among adsorbate molecules, signifying a behavior in which the interaction of the adsorbate with an already adsorbed layer is stronger than the interaction between the solid surface and the adsorbate. It is represented by Eq. (20) [41]

$$\frac{t}{q_t} = \frac{1}{k_2 q_e^2} + \frac{t}{q_e} \tag{20}$$

The IPD defines the process by which adsorbate (Pb^{2+}) molecules are adsorbed onto the active sites within the particles. The interaction is controlled by the energetic interactions between the adsorbate and the adsorbent. The IPD equation is [41]

$$q_t = k_3 t^{1/2} + C \tag{21}$$

where k_1, k_2 and k_3 are the PFO, PSO and IPD rate constants in (min^{-1}) and (g/mg.min), respectively. If the obtained data agrees with pseudo-first-order reaction, the adsorption tends more towards physisorption. Physisorption is weak and reversible. However, the pseudo-second order reaction is stronger as it occurs through bond formation formed between the adsorbent and adsorbate by electron sharing.

On the other hand, Fig. 12 illustrates a representative graph of the previous models for $BaFe_{11.5}Zr_{0.5}O_{19}$, while other graphs are not included here. The calculated data for each model corresponding to the prepared samples are detailed in Table 3. The regression values of LIM and FIM show that the LIM is well suited and favorable for adsorption of Pb^{2+}, indicating, a monolayer-type adsorption. An analysis of the adsorption mechanism through the three models, along with the calculation of regression values for each, reveals that $BaFe_{11.5}Zr_{0.5}O_{19}$ adheres to the intra-particle diffusion model. In contrast, $BaFe_{11.5}Zn_{0.5}O_{19}$, $BaFe_{11.5}Ni_{0.5}O_{19}$, and $BaFe_{11.5}Gd_{0.5}O_{19}$ conform to the principles of the PSO model. This indicates that the adsorption mechanism is chemically driven [43].

Finally, it can be detected that the adsorption efficiency of $BaFe_{11.5}Zr_{0.5}O_{19}$ is higher compared to doped $BaFe_{12}O_{19}$, and this conclusion is proved by BET analysis shown in Fig. 12g. An empirical classification of hysteresis loops was given by IUPAC, which is based on an earlier classification of hysteresis by de Boer [43]. Accordingly the hysteresis in Fig. 12f is classified as type H3 associated with a type II isotherm [43]. The pores of sample are categorized based on their diameter into micropores (<2 nm), mesopores (ranging from 2 to 50 nm), and macropores (>50 nm). In the studied samples the inter particle pores are identified as mesopores as illustrated in Fig. 12g.

4 Conclusion

$BaFe_{11.5}Gd_{0.5}O_{19}$ exhibited the smallest crystallite size, measuring 35.328 nm, and 36.968 nm according to the MSM, and HWM respectively. This finding was further validated by assessing the strain through the Halder-Wagner model, which indicated the lowest strain value of $0.726*10^{-3}$.

The data obtained has demonstrated that $BaFe_{11.5}Zr_{0.5}O_{19}$ exhibits the highest porosity, attributed to the significant molar mass of Zr, making it suitable for wastewater treatment applications. The analysis of the data reveals that $BaFe_{11.5}Zr_{0.5}O_{19}$ exhibited the highest energy bandgap, measuring 1.728 eV according to the Kubelka–Munk relation and 1.590 eV based on the ASF relation. Doping the crystal structure with Zr^{4+}, Gd^{3+}, Zn^{2+} and Ni^{2+} cations modifies the critical aspects of the sample's optical band structure. Such adjustments make BHF a valuable component for numerous technological uses.

For each sample, a rapid elimination of Pb^{2+} ions within the initial 30 min of adsorption has been observed, with removal efficiencies of 99.693%, 93.098%, 92.382%, and 99.237% for $BaFe_{11.5}Zr_{0.5}O_{19}$, $BaFe_{11.5}Zn_{0.5}O_{19}$, $BaFe_{11.5}Ni_{0.5}O_{19}$, and $BaFe_{11.5}Gd_{0.5}O_{19}$, respectively.

The adsorption mechanism analyzed through the three models, along with the calculation of regression values for each, reveals that $BaFe_{11.5}Zr_{0.5}O_{19}$ follows the intra particle

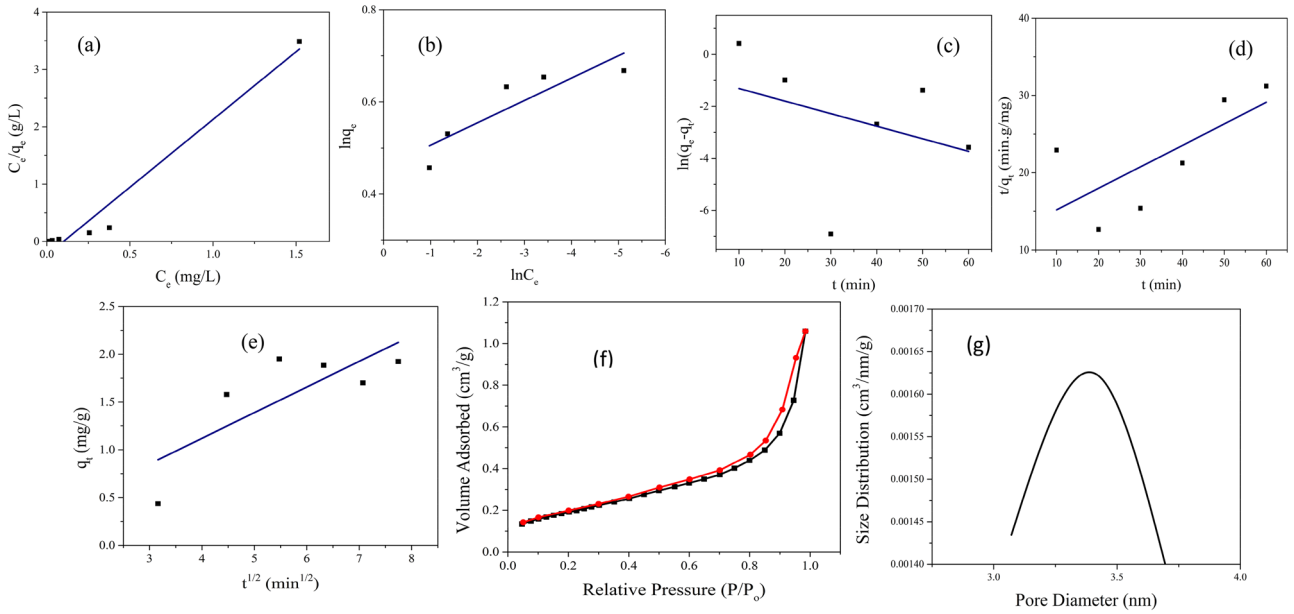

Fig. 12 **a**–**g** Graphs of adsorption mechanism models for $BaFe_{11.5}Zr_{0.5}O_{19}$: **a** LIM, **b** FIM, **c** PFO model, **d** PSO model, **e** IPD model, **f** BET analysis and **g** Pore width

diffusion model. In contrast $BaFe_{11.5}Zn_{0.5}O_{19}$, $BaFe_{11.5}Ni_{0.5}O_{19}$ and $BaFe_{11.5}Gd_{0.5}O_{19}$ follow the pseudo-second-order model rules, suggesting that their adsorption mechanisms are chemically in nature.

Finally, the interaction among electronic configuration, ionic radii, and optical energy gap presents a vital aspect in defining the characteristics of BHF NPs, particularly within the domains of materials science and solid-state physics.

Data availability

All data that support the findings of this study are included within the article (and any supplementary files).

Author contributions Ebtesam E Ateia contributed with conceptualization, validation, data gathering and analysis, writing and preparing the original draft, supervision, visualization, reviewing, and editing. Yousra Yasser contributed to the preparation of the material, the gathering and analysis of data, formal analysis, inquiry, methodology, validity and visualization. Amira S Shafaay contributed with material preparation, data curation, analysis, research, methodology, formal analysis, supervision, validity and visualization.

Funding Open access funding provided by The Science, Technology & Innovation Funding Authority (STDF) in cooperation with The Egyptian Knowledge Bank (EKB).

Compliance with ethical standards

Conflict of interest The authors declare no competing interests.

Publisher's note Springer Nature remains neutral with regard to jurisdictional claims in published maps and institutional affiliations.

References

1. Wang S et al. (2021) M-type barium hexaferrite nanoparticles synthesized by γ-ray irradiation assisted polyacrylamide gel method and its optical, magnetic and super capacitive performances. J Clust Sci 32:569–578. https://doi.org/10.1007/s10876-020-01815-6
2. Ateia EE, Rabie O, Mohamed AT (2023) Multi-susceptible single-phased hexaferrite with significant magnetic switching properties by selectively doping. Phys Scr 98, https://doi.org/10.1088/1402-4896/acd230.
3. Manglam MK, Kumari S, Mallick J, Kar M (2021) Crystal structure and magnetic properties study on barium hexaferrite of different average crystallite size. Appl Phys A Mater Sci Process, 127, https://doi.org/10.1007/s00339-020-04232-8
4. Verma S et al. (2021) Understanding the phase evolution with temperature in pure ($BaFe_{12}O_{19}$) and zinc-zirconium co-doped barium hexaferrite (BaZnZrFe10O19) samples using Pawley and Rietveld analysis. Mater Today Commun 27, https://doi.org/10.1016/j.mtcomm.2021.102291.
5. Mahapatro J, Agrawal S (2022) Optical, dielectric and electrical properties of Gd^{3+} ions doped barium hexaferrite ceramic

compounds for microwave device applications. J Alloys Compd 907, https://doi.org/10.1016/j.jallcom.2022.164405.
6. Ateia EE, Yasser Y, Shafaay AS (2025) Multi-substituted barium hexaferrite with magnetoplumbite structure for microwave high-frequency applications. J Solgel Sci Technol 115:98–114. https://doi.org/10.1007/s10971-025-06783-9.
7. Pazhani N, Velavan R (2020) Microstructure and properties of barium hexaferrite nanoparticles. Malaya J Matematik S:4960–4965. https://doi.org/10.26637/MJM0S20/1279.
8. Himanshi et al. (2023) Synthesis, characterization, and applications of doped barium hexaferrites: a review, Physica B Condens Matter 667, https://doi.org/10.1016/j.physb.2023.415202.
9. Nuraini U, Amalia L, Rosyidah KC, Zainuri M (2015) Crystal structure and magnetic properties of Zn doped barium M-hexaferrite. Adv Mat Res 1112:19–22.
10. Ateia EE, Rabie O, Mohamed AT (2024) Magneto-fluorescent core–shell $Sr_{0.8}La_{0.2}Fe_{11}CuO_{19}$ @ CQDs for the detection of metal ions. Appl Surf Sci 678, https://doi.org/10.1016/j.apsusc.2024.161123
11. Ateia EE, Fouad S, Mohamed AT (2025) Characterization of spinel ferrite nano composites: from synthesis to application. Appl Phys A Mater Sci Process 131:980
12. Masindi V, Muedi KL (2018) Environmental contamination by heavy metals. In: Heavy metals. InTech, https://doi.org/10.5772/intechopen.76082.
13. Saeid YA, Ateia EE (2022) Efficient removal of Pb (II) from water solution using $CaFe_{2-x-y}Gd_xSm_yO_4$ ferrite nanoparticles. Appl Phys A Mater Sci Process 128, https://doi.org/10.1007/s00339-022-05718-3
14. Reda M, Ateia EE, El-Dek SI, Arman MM (2024) New insights into optical properties, and applications of Zr-doped $BaTiO_3$. Appl Phys A Mater Sci Process 130, https://doi.org/10.1007/s00339-024-07381-2
15. Ateia EE, Elsayed K, Ramadan R (2022) Tuning the properties of Ba-M hexaferrite $BaFe_{11.5}Co_{0.5}O_{19}$: a road towards diverse applications. J Inorg Organomet Polym Mater 32:2502–2512. https://doi.org/10.1007/s10904-022-02341-w
16. Salah TA, Mohammad AM, Hassan MA, El-Anadouli BE (2014) Development of nano-hydroxyapatite/chitosan composite for cadmium ions removal in wastewater treatment. J Taiwan Inst Chem Eng 45:1571–1577. https://doi.org/10.1016/j.jtice.2013.10.008
17. Singh K, Renu NA, Agarwal M (2017) Methodologies for removal of heavy metal ions from wastewater: an overview. Interdiscip Environ Rev 18:124. https://doi.org/10.1504/ier.2017.10008828
18. Dhage VN, Mane ML, Keche AP, Birajdar CT, Jadhav KM (2011) Structural and magnetic behaviour of aluminium doped barium hexaferrite nanoparticles synthesized by solution combustion technique. Phys B Condens Matter 406:789–793. https://doi.org/10.1016/j.physb.2010.11.094
19. Pullar RC (2012) Hexagonal ferrites: a review of the synthesis, properties and applications of hexaferrite ceramics. https://doi.org/10.1016/j.pmatsci.2012.04.001.
20. Ateia EE, Ramadan R, Shafaay AS (2020) Efficient treatment of lead-containing wastewater by $CoFe_2O_4$/graphene nanocomposites. Appl Phys A Mater Sci Process 126, https://doi.org/10.1007/s00339-020-3401-3
21. Jing XD, Li ZG, Chen ZT, Li ZY, Qin CY, Gong HY (2023) Effect of praseodymium valence change on the structure, magnetic, and microwave absorbing properties of M-type strontium ferrite: the mechanism of influence of citric acid dosage and calcination temperature. Mater Today Chem 30, https://doi.org/10.1016/j.mtchem.2023.101537
22. Mohammad AM, Salah Eldin TA, Hassan MA, El-Anadouli BE (2017) Efficient treatment of lead-containing wastewater by hydroxyapatite/chitosan nanostructures. Arab J Chem 10:683–690. https://doi.org/10.1016/j.arabjc.2014.12.016.
23. Ateia EE, Reda M, El-Dek SI, Arman MM (2024) A comparative approach for estimating microstructural characteristics of $BaTi_{1-x}Zr_xO_3$ ($0.0 \le x \le 0.3$) nanoparticles via X-ray diffraction patterns. J Sol Gel Sci Technol 110:887–899. https://doi.org/10.1007/s10971-024-06389-7.
24. Muhiuddin G et al. (2023) Synthesis of Ni doped barium hexaferrite by microemulsion route to enhance the visible light-driven photocatalytic degradation of crystal violet dye. Ceram Int 49:4342–4355. https://doi.org/10.1016/j.ceramint.2022.09.319.
25. Shidaye MN et al. (2023) Nano structural engineering of Ba-substituted Sr-hexaferrites for viable microwave absorbance and magnetic data storage. Phys B Condens Matter 666, https://doi.org/10.1016/j.physb.2023.415125.
26. Joshi H, Ruban Kumar A (2023) Divalent Cation Substitution Impact on the Properties of Strontium Aluminium Hexaferrite ($SrAl_2$ Fe_{10} O_{19}). Available: https://ssrn.com/abstract=4409497
27. Souri D, Tahan ZE (2015) A new method for the determination of optical band gap and the nature of optical transitions in semiconductors. Appl Phys B 119:273–279. https://doi.org/10.1007/s00340-015-6053-9.
28. Sehar F, Anjum S, Mansoor A, Mustafa Z (2021) Formation of non-centrosymmetric covalent bonds due to the substitution of cobalt contents in M-type barium hexa-ferrites $BaFe_{(12-x)}O_{19}$. Appl Phys A Mater Sci Process 127, https://doi.org/10.1007/s00339-021-04762-9
29. Souri D, Shomalian K (2009) Band gap determination by absorption spectrum fitting method (ASF) and structural properties of different compositions of (60-x) V_2O_5-40TeO_2-xSb_2O_3 glasses. J Non Cryst Solids 355:1597–1601. https://doi.org/10.1016/j.jnoncrysol.2009.06.003
30. Ateia EE, Saeid YA (2024) Characterization of core–shell $CaFe_{1.925}Sm_{0.05}Gd_{0.025}O_4$ @ polymer from synthesis to applications. J Inorg Organomet Polym Mater 34:118–130. https://doi.org/10.1007/s10904-023-02799-2
31. Rostami M, Jafarpour M, Majles Ara MH (2021) An investigation on the microwave absorption properties of Co–Al–Ti substituted barium hexaferrite-MWCNT nanocomposites, J Alloys Compd 872, https://doi.org/10.1016/j.jallcom.2021.159656
32. Subramanyam G, Rao NK, Daivajna MD (2024) La3+-induced band-gap modifications in barium hexaferrite: an investigation of the structural, optical, and dielectric properties. Eng Proc 55, https://doi.org/10.3390/engproc2023055094
33. Rane MV, Bahadur D, Nigam AK, Srivastava CM (1999) Mossbauer and FT-IR studies on non-stoichiometric barium hexaferrites. J Magn Magn Mater 192(2), 288–296
34. Singh VP et al. (2018) A current review on the synthesis and magnetic properties of M-type hexaferrites material. World J Condens Matter Phys 08:36–61. https://doi.org/10.4236/wjcmp.2018.82004.
35. Asif SU et al. (2023) Structural and magnetic influence by mg on $BaFe_{10}Al_2O_{19}$ hexaferrites prepared via ceramic route for potential magnetic applications. J Mater Sci 34, https://doi.org/10.1007/s10854-023-11645-7.
36. Lemziouka et al. (2020) Synthesis, structural, optical and dispersion parameters of La-doped spinel zinc ferrites ZnFe2-xLaxO4 (x = 0.00, 0.001, 0.005, 0.01 and 0.015). Vacuum 182, https://doi.org/10.1016/j.vacuum.2020.109780
37. Okamura H (2012) A simple method for the Kramers-Kronig analysis of reflectance spectra measured with diamond anvil cell. J Phys, https://doi.org/10.1088/1742-6596/359/1/012013
38. Silaeva E, Saddier L, Colombier JP (2021) Drude–lorentz model for optical properties of photoexcited transition metals under electron–phonon nonequilibrium. Appl Sci 11 https://doi.org/10.3390/app11219902
39. Polat O, Caglar M, Coskun FM, Coskun M, Caglar Y, Turut A (2020) An investigation of the optical properties of $YbFe_{1-x}Ir_xO_{3-\delta}$ (x=0, 0.01 and 0.10) orthoferrite films. Vacuum, 173, https://doi.org/10.1016/j.vacuum.2019.109124.

40. Ateia EE, Gawad D, Arman MM (2024) Core-shell nanomaterials based on La_2FeCrO_6 coated with metal oxides for optical applications. Phys Scr 99, https://doi.org/10.1088/1402-4896/ad80e6
41. Mohammad AM, Salah Eldin TA, Hassan MA, El-Anadouli BE (2017) Efficient treatment of lead-containing wastewater by hydroxyapatite/chitosan nanostructures. Arab J Chem 10:683–690
42. Mahmood M, Iqbal S, Jamshaid M, Kalsoom A, Al-Mohaimeed AM, Iqbal R, Bibi F, Raza Q, Elshikh MS (2024) Efficient tetracycline removal from hospital wastewater using visible light active M-type lead hexaferrite/g-C_3N_4 composites. J Sol Gel Sci Tech 112:801–813
43. Himanshi R, Jasrotia B, Lal N, Lakshmaiya J, Ahmed S, Kandwal A, Saad M (2025) Alshehri" Sol-gel fabricated barium M-type hexaferrites: Effect of high cobalt doping on the structural, optical, surface, and magnetic traits of $BaFe_{12}O_{19}$ hexaferrites. J Sol Gel Sci Tech 115:1497–1509